Photochemistry of HOx in the upper troposphere at northern midlatitudes

Citation

Published Version

Permanent link

http://nrs.harvard.edu/urn-3:HUL.InstRepos:14121770

Terms of Use

Share Your Story

Photochemistry of HO_x in the upper troposphere at northern midlatitudes

L. Jaeglé,[1] D. J. Jacob,[1] W. H. Brune,[2] I. Faloona,[2] D. Tan,[2] B. G. Heikes,[3] Y. Kondo,[4] G. W. Sachse,[5] B. Anderson,[5] G. L. Gregory,[5] H. B. Singh,[6] R. Pueschel,[6] G. Ferry,[6] D. R. Blake,[7] and R. E. Shetter[8]

Abstract. The factors controlling the concentrations of HO_x radicals (= OH + peroxy) in the upper troposphere (8-12 km) are examined using concurrent aircraft observations of OH, HO_2, H_2O_2, CH_3OOH, and CH_2O made during the Subsonic Assessment Ozone and Nitrogen Oxide Experiment (SONEX) at northern midlatitudes in the fall. These observations, complemented by concurrent measurements of O_3, H_2O, NO, peroxyacetyl nitrate (PAN), HNO_3, CH_4, CO, acetone, hydrocarbons, actinic fluxes, and aerosols, allow a highly constrained mass balance analysis of HO_x and of the larger chemical family HO_y (= HO_x + 2 H_2O_2 + 2 CH_3OOH + HNO_2 + HNO_4). Observations of OH and HO_2 are successfully simulated to within 40% by a diel steady state model constrained with observed H_2O_2 and CH_3OOH. The model captures 85% of the observed HO_x variance, which is driven mainly by the concentrations of NO_x (= NO + NO_2) and by the strength of the HO_x primary sources. Exceptions to the good agreement between modeled and observed HO_x are at sunrise and sunset, where the model is too low by factors of 2-5, and inside cirrus clouds, where the model is too high by factors of 1.2-2. Heterogeneous conversion of NO_2 to HONO on aerosols ($\gamma_{NO2}=10^{-3}$) during the night followed by photolysis of HONO could explain part of the discrepancy at sunrise. Heterogeneous loss of HO_2 on ice crystals ($\gamma_{ice\_HO2}=0.025$) could explain the discrepancy in cirrus. Primary sources of HO_x from $O(^1D)+H_2O$ and acetone photolysis were of comparable magnitude during SONEX. The dominant sinks of HO_y were $OH+HO_2$ ($NO_x<50$ parts per trillion by volume (pptv)) and $OH+HNO_4$ ($NO_x>50$ pptv). Observed H_2O_2 concentrations are reproduced by model calculations to within 50% if one allows in the model for heterogeneous conversion of HO_2 to H_2O_2 on aerosols ($\gamma_{HO2}=0.2$). Observed CH_3OOH concentrations are underestimated by a factor of 2 on average. Observed CH_2O concentrations were usually below the 50 pptv detection limit, consistent with model results; however, frequent occurrences of high values in the observations (up to 350 pptv) are not captured by the model. These high values are correlated with high CH_3OH and with cirrus clouds. Heterogeneous oxidation of CH_3OH to CH_2O on aerosols or ice crystals might provide an explanation ($\gamma_{ice\_CH3OH}\sim0.01$ would be needed).

1. Introduction

The Subsonic Assessment Ozone and Nitrogen Oxide Experiment (SONEX) aircraft campaign over the north Atlantic in October-November 1997 provided the first concurrent measurements in the upper troposphere of HO_x

radicals (HO_x = OH + peroxy) and of the ensemble of species thought to control HO_x production and loss: H_2O_2, CH_3OOH, CH_2O, O_3, H_2O, HNO_3, CH_4, acetone and hydrocarbons. The goal of SONEX was to assess the impact of aircraft emissions on the concentrations of nitrogen oxides (NO_x = NO + NO_2) and ozone production in the upper troposphere [*Singh et al.*, this issue]. A major step toward that goal was to understand the chemistry of HO_x, which drives ozone production. An analysis of the photochemistry of ozone production during SONEX, based on the concurrent observations of HO_x and NO_x, is presented by *Jaeglé et al.* [1999].

We use here the SONEX observations to evaluate our current understanding of HO_x chemistry in the upper troposphere and to introduce some new ideas regarding the role of heterogeneous chemistry. We define the chemical family HO_y including HO_x radicals and their non radical reservoirs (HO_y = HO_x + 2 H_2O_2 + 2 CH_3OOH + HNO_2 + HNO_4). The factors controlling HO_y concentrations in the upper troposphere can then be separated into four elements [*Jaeglé et al.*, 1997]: (1) primary HO_x sources (H_2O, acetone, and convective injection of HO_x precursors [*Chatfield and Crutzen*, 1984; *Prather and Jacob*, 1997; *Jaeglé et al.*, 1997;

[1]Division of Engineering and Applied Sciences and Department of Earth and Planetary Sciences, Harvard University, Cambridge, Massachussetts.
[2]Department of Meteorology, Pennsylvania State University, University Park.
[3]Graduate School of Oceanography, University of Rhode Island, Narragansett.
[4]Solar Terrestrial Environment Laboratory, Nagoya University, Nagoya, Japan.
[5]NASA Langley Research Center, Hampton, Virginia.
[6]NASA Ames Research Center, Moffett Field, California.
[7]Department of Chemistry, University of California, Irvine.
[8]National Center for Atmospheric Research, Boulder, Colorado.

Table 1. Instruments on Board the DC-8 Aircraft During SONEX (October 13 to November 12, 1997)

Variable	Time Resolution	LOD	Accuracy	Technique	Reference
OH	60 s	0.03 pptv	40%	laser induced fluorescence	*Stevens et al.* [1994]
HO$_2$	60 s	0.12 pptv	40%	laser induced fluorescence	*Stevens et al.* [1994]
H$_2$O$_2$	2-3 min	15 pptv	15 pptv	high-pressure liquid chromatograph	*Lee et al.* [1995]
CH$_3$OOH	2-3 min	25 pptv	25 pptv	high-pressure liquid chromatograph	*Lee et al.* [1995]
CH$_2$O	5 min	50 pptv	25 pptv	fluorometry	*Heikes et al.* [1996]
H$_2$O	1 s	0.2 ppmv	10%	tunable diode laser hygrometer	*Vay et al.* [1998]
O$_3$	1 s	<2 ppbv	5%	NO-O$_3$ chemiluminescence	*Gregory et al.* [1983]
CO	1 s	1 ppbv	2%	diode laser spectrometer	*Sachse et al.* [1991]
CH$_4$	1 s	2 ppbv	1%	diode laser spectrometer	*Sachse et al.* [1991]
NO	10 s	3 pptv	13%	chemiluminescence	*Kondo et al.* [1999]
HNO$_3$	5-10 min	<20 pptv	10-20%	mist chamber technique	*Talbot et al.* [1999]
PAN	2 min	1 pptv	20%	GC/ECD[a]	*Singh et al.* [this issue]
Acetone	2.5 min	15 pptv	25%	gas chromatograph	*Singh et al.* [this issue]
C$_2$-C$_{10}$ NMHCs	3-4 min	2 pptv	2-10%	GC/ECD/FID[a]	*Simpson et al.* [this issue]
Actinic flux (280-420 nm)	30 s	80 photons/ (cm^2 s nm)	8-12%	upwelling and downwelling spectroradiometers	*Shetter and Müller* [1999]

Only the instruments and measured parameters used for this study are listed.

[a]Gas chromatograph (GC) with electron capture detection (ECD) and flame ionization detection (FID).

Wennberg et al., 1998]), (2) amplification of these primary sources through methane oxidation and the photolysis of CH$_2$O, (3) chemical cycling between HO$_x$ and its HO$_y$ reservoirs, and, (4) loss of HO$_y$. For the first time we can quantify and examine each of these elements based on observations.

2. Observations

A complete list of measurements on board the SONEX DC-8 aircraft is given by *Singh et al.* [1999]. Table 1 shows the subset of measurements used in the present analysis. Fourteen flights were conducted out of four locations: NASA Ames Research Center in California (37°N, 121°W), Bangor in Maine (45°N, 69°W), Shannon in Ireland (53°N, 9°W), and Lajes in the Azores (39°N, 27°W). Figure 1 shows the aircraft flight tracks. Most were in the upper troposphere between 8 and 12 km. The average tropopause height varied from 14 km south of 30°N to 10 km north of 60°N.
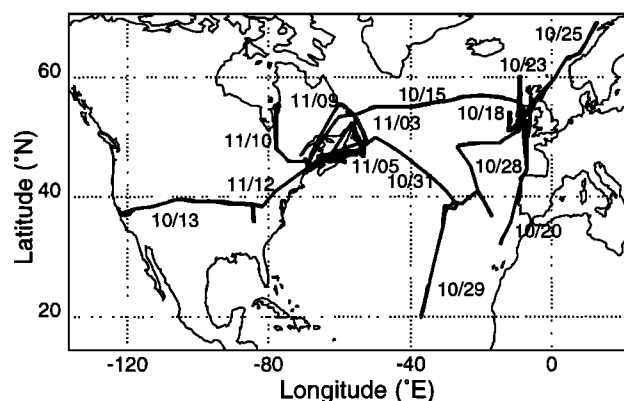

Figure 1. Flight tracks during SONEX (October 13 to November 12, 1997). Flight dates are indicated next to the tracks.

Each instrument collected data with a different time resolution (Table 1), and analyzing these observations together requires merging them on a common time interval. We generally choose to average the data over the sampling time of the critical variable with the coarsest temporal resolution. For the analysis presented here, we use three different types of merged data sets based on the time intervals of (1) the peroxides measurement (2-3 min), (2) the CH$_2$O measurement (5 min), and (3) a constant 1-min interval. We focus our attention on measurements taken at 8-12 km altitude, representing 80% of the entire SONEX data set.

The aircraft sampled air masses of various origins at 8-12 km which we classify into six different categories: (1) stratospheric influence, (2) tropical marine convection, (3) midlatitude marine convection, (4) continental convection, (5) cirrus clouds, and (6) background. Median concentrations for each category are summarized in Table 2. Observations impacted by fresh aircraft exhaust are excluded from this table. Classification criteria and characteristics of each category are presented below.

We define air masses as having a stratospheric influence if ozone is more than 90 ppbv and CH$_4$ less than 1760 ppbv. This threshold of 90 ppbv is based on ozone sonde measurements at the tropopause for northern midlatitudes fall [*Logan*, 1994]. In these air masses the median O$_3$, CO and H$_2$O concentrations were of 149 ppbv, 53 ppbv, and 42 ppmv, consistent with a stratospheric influence. The highest ozone concentrations observed were 450 ppbv.

Marine air recently transported by convection to the upper troposphere is diagnosed on the basis of the concentrations of CH$_3$I and acetylene C$_2$H$_2$. CH$_3$I, which has a lifetime of 5-10 days in the upper troposphere during SONEX, has been used in previous studies as a tracer for marine convection [*Cohan et al.*, 1999; S.C. Liu et al., Vertical transport over the tropics: implications for ozone distribution and photochemistry, submitted to *Journal of Geophysical Research*, 1999]. C$_2$H$_2$ is generally associated with continental polluted air. Low levels of C$_2$H$_2$ (<75 parts per trillion by volume (pptv)) and

Table 2. Median Concentrations of Species Observed During SONEX (October 13 to November 12, 1997) Between 8 and 12 km Altitude Classified According to Air Mass Origin

	Background	Stratospheric Influence	Air Mass Convection Tropical Marine	Air Mass Convection Midlatitude Marine	Air Mass Convection Continental	Cirrus
Percent of measurements in the UT[a]	50%	17%	6%	6%	6%	14%
Temperature, K	227	223	225	231	223	231
Pressure, mbar	287	239	261	303	262	287
H$_2$O, ppmv	120	42	195	208	128	388
Relative humidity (ice), %	64	25	93	75	101	114
Relative humidity (liquid), %	42	15	59	48	62	75
OH, pptv	0.08	0.071	0.11	0.077	0.085	0.075
HO$_2$, pptv	2.2	1.2	4.7	2.7	1.1	2.7
H$_2$O$_2$, pptv	78	24	153	85	38	97
CH$_3$OOH, pptv	<25	<25	68	89	<25	55
CH$_2$O, pptv	<50	<50	<50	<50	70	78
NO, pptv	56	65	49	40	443	33
NO$_2$,[b] pptv	30	55	11	18	163	22
NO$_x$,[b] pptv	93	135	60	68	593	83
HNO$_4$,[b] pptv	60	68	40	56	63	64
HNO$_3$, pptv	120	570	44	61	130	67
PAN, pptv	64	54	29	70	55	68
NO$_y$, pptv	330	800	190	280	880	300
O$_3$, ppbv	55	149	33	47	55	50
CH$_4$, ppbv	1761	1732	1745	1766	1761	1765
CO, ppbv	90	53	75	85	92	96
Ethane, pptv	670	410	600	740	720	730
Propane, pptv	79	28	73	140	110	110
Acetylene, pptv	91	41	55	98	110	110
Benzene, pptv	15	3	10	25	14	23
HCOOH, pptv	37	35	23	25	21	33
CH$_3$COOH, pptv	<27	<41	<21	<22	<27	<26
Methanol, pptv	380	86	390	440	380	470
Acetone, pptv	510	300	530	510	560	550
CHBr$_3$, pptv	0.51	0.12	0.71	0.98	0.84	0.95
CH$_3$I, pptv	0.12	0.062	0.35	0.35	0.11	0.33
Condensation nuclei, cm^{-3}	3000	1500	6000	5200	17500	2800
Aerosol surface area,[c] μm^{2}cm^{-3}	7.8	8.1	4.4	10	11.4	27.8
SA_1,[c] μm^2 cm^{-3}	0.047	0.017	0.092	0.12	0.62	0.074
SA_2,[c] μm^2 cm^{-3}	3	0.75	3.8	3.2	3.6	2.4
SA_3,[c] μm^2 cm^{-3}	3	4.7	0.42	5.6	5	7
SA_4,[c] μm^2 cm^{-3}	0.016	0	0.016	0.92	0.48	28.9

Observations below their limit of detection are included in this table. We indicate when the median is below the limit of detection.

[a] The remaining 1% correspond to observations in fresh aircraft exhaust (not shown in this table).

[b] Model calculated values. NO$_x$ = NO(obs.) + NO$_2$(model).

[c] Total surface area for aerosols with diameters between 0.004 and 24 μm. SA_1, SA_2, SA_3, and SA_4 correspond respectively to aerosol surface areas in the 0.004-0.015, 0.015-0.1, 0.1-3, and 3-24 μm diameter size ranges.

high levels of CH$_3$I (>0.25 pptv) are interpreted as resulting from convection of clean marine air, possibly of tropical origin [*Grant et al.*, this issue; *Thompson et al.*, 1999]; while higher levels of C$_2$H$_2$ with high levels of CH$_3$I are interpreted as convection of midlatitude marine air, with some influence from polluted continental sources as previously observed by *Parrish et al.* [1998]. We classify these two categories as tropical and midlatitude marine convection. Other species confirmed this difference between tropical and midlatitude marine air masses, including benzene (10 pptv for tropical and 25 pptv for midlatitude) and ozone (33 and 47 ppbv). High relative humidity over ice (93% and 75%), high levels of

CHBr$_3$ (0.71 and 0.98 pptv) and relatively low levels of NO$_x$ (60 and 68 pptv) accompany both types of air masses.

Elevated NO$_x$/NO$_y$ concentration ratios and NO$_y$ concentrations (NO$_x$/NO$_y$>0.5 mol/mol and NO$_y$>500 pptv) extending over large spatial scales (>20-50 km) are interpreted as resulting from recent lightning and convective transport of NO$_x$ from the polluted boundary layer [*Thompson et al.*, 1999; K.E. Pickering et al., unpublished manuscript, 1999]. We refer to this category as continental convection to contrast it to the two marine convection categories with low NO$_x$. Satellite-derived lightning data show frequent occurrences of lightning discharges upwind of the SONEX

region in the Gulf of Mexico, Gulf Coast states, off the east coast of the United States, and over the central subtropical Atlantic Ocean [*Fuelberg et al.*, this issue]. All three types of convectively influenced air masses contain elevated levels of condensation nuclei (CN) (Table 2), possibly resulting from recent nucleation in air where large particles have been rained out [*Clarke*, 1992].

Measurements inside cirrus clouds are diagnosed from the presence of supermicron aerosols (from 3 to 24 μm) at concentrations larger than 10^{-4} cm^{-3}. This diagnosis was verified by viewing the videotapes recorded by on board cameras. For the two flights when no measurements of aerosols were collected (October 13 and November 12), we use the videotapes to determine the occurrence of measurements inside clouds. Many of the cirrus clouds sampled were part of marine convective outflows as shown by high levels of CH_3I and $CHBr_3$ (0.33 pptv and 0.95 pptv).

Air masses impacted by fresh aircraft exhaust were identified from the occurrence of many spikes of elevated NO (>100 pptv above background) and CN lasting a few seconds. These spikes were indicative of crossings of aircraft plumes [*Kondo et al.*, 1999].

With the above classification, we find that in the upper troposphere during SONEX, convection affected 18% of the observations (6% tropical marine, 6% midlatitude marine, 6% continental), measurements inside cirrus clouds occurred 14% of the time, air with stratospheric influence was sampled for 17% of the cases, and fresh aircraft emissions impacted the observed air for 1% of the data collected. Upper tropospheric air not included in any of the above categories was classified as "background" air (50% of the cases).

The aerosol surface area was calculated by combining measurements from four different instruments on board the DC-8: two condensation nuclei counters measuring particles in the 0.004-1 μm and 0.015-1 μm diameter ranges [*B. Anderson et al.*, 1999], and two size-resolved aerosol probes measuring particles in the 0.1-3 μm and 0.42-24 μm diameter ranges [*Pueschel et al.*, this issue]. The two CN counters are total aerosol counters, and to obtain size distribution information, we use the data from the Mobile Aerosol Sampling system measuring particles between 0.001 and 0.1 μm [*Hagen et al.*, 1992] on board the Falcon aircraft during the parallel Pollution from Aircraft Emissions in the North Atlantic Corridor (POLINAT 2) campaign. The resulting median aerosol surface area was of 8 $μm^2$ cm^{-3} during SONEX, with roughly equal contributions from aerosols in the 0.015-0.1 μm range and in the 0.1-3 μm range.

3. Model

Our analysis of the SONEX data is based on a zero-dimensional (0-D) photochemical model including a detailed mechanism for HO_x-NO_x-hydrocarbon chemistry in the troposphere [*Jaeglé et al.*, 1997; *Schultz et al.*, 1999]. Chemical species are divided in two categories; constrained and calculated. Concentrations of constrained species are specified from observations along the flight tracks, while calculated species are assumed to be in a diel steady state defined by reproducibility of concentrations over a 24-hour solar cycle. Constrained species include O_3, NO, H_2O, peroxyacetyl nitrate (PAN), HNO_3, CO, CH_4, ethane, propane, C_4 alkanes, and acetone. Other constrained variables

specified from observations include aerosol surface area, temperature, pressure, and actinic flux. The concentration of NO_t (= NO + NO_2 + NO_3 + 2 N_2O_5 + HNO_4) is calculated in the model such that the calculated NO matches the observed NO at the time of day of observations [*Jacob et al.*, 1996]. The minimum requirement for a calculation to be performed at a given point is that observations of O_3, NO, H_2O, CO, temperature, and pressure be available. If PAN, HNO_3, CH_4, acetone, or any hydrocarbon were not measured, we use an interpolation based on observations collected during the rest of the flight.

The most constrained model calculation of OH and HO_2 is obtained when in addition to all the above parameters, observations of H_2O_2, CH_3OOH, and CH_2O are also available as constraints. Because of the scarcity of CH_2O and CH_3OOH observations above their limits of detection (LOD) (50 pptv for CH_2O, 25 pptv for CH_3OOH), and the long integration time of CH_2O (5 min), this calculation is possible for only 45 points in the merged data set averaged over the CH_2O measurement interval. If we relax the constraint on CH_2O measurement availability and instead assume CH_2O to be in diel steady state, we enable model calculations for 540 points in the merged data set averaged over the peroxide measurement time step. Further assuming steady state for CH_3OOH when observations are below the LOD increases sample size to 820 points. We refer to this model calculation as the "standard" model. The suitability of the chemical steady state assumption for CH_2O and CH_3OOH will be examined separately.

The chemical mechanism in the model is based on the recommendations of *DeMore et al.* [1997] and *Atkinson et al.* [1997], with a few updates including temperature-dependent cross sections and pressure-dependent quantum yields for acetone photolysis [*Gierczak et al.*, 1998], $O(^1D)$ quantum yield from ozone photolysis [*Talukdar et al.*, 1998], and rate constant for the $OH+NO_2$ reaction [*Dransfield et al.*, 1999].

Hydrolysis of N_2O_5 in aerosols is included with a reaction probability γ_{N2O5} = 0.1 [*DeMore et al.*, 1997]. We also include reaction of HO_2 in aerosols [*Hanson et al.*, 1992; *Cooper and Abbatt*, 1996]. Following the recommendation of *Jacob* [1999], we assume that the uptake of HO_2 by the aerosols can be described by first-order kinetics with γ_{HO2} = 0.2 and the stoichiometry

(R1) HO_2 + aerosol → ½ H_2O_2 + ½ O_2 .
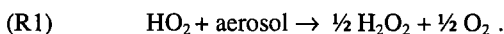
These reaction probabilities are applicable only for aqueous aerosols; for dry aerosols they are considerably less [*Jacob*, 1999]. Bulk aerosol composition measurements during SONEX indicated frequent neutralization of SO_4^{2-} by NH_4^+ (J. Dibb, personal communication, 1999), in which case the sulfate aerosol would be dry at phase equilibrium [*Martin*, 1998]. However, the high relative humidities (42% median relative humidity over liquid water) should allow the aerosol to remain in a metastable aqueous form [*Cziczo and Abbatt*, 1999]. We have assumed the aerosol to be aqueous at all relative humidities.

In order to model observations inside cirrus clouds we consider the same reactions as for aqueous aerosols, but with lower reaction probabilities: γ_{ice_N2O5} = 0.01 and γ_{ice_HO2} = 0.025 [*DeMore et al.*, 1997]. The largest aerosol size bin measured on the DC-8 extended to 24 μm, thus not sampling all the cirrus particles, which can have diameters larger than

100 μm. In order to test the effect of heterogeneous chemistry on cirrus, we conduct sensitivity calculations for a range of assumed surface areas.

Spectrally resolved 280-420 nm actinic fluxes were measured during SONEX by *Shetter and Müller* [1999] with a resolution of 1-2 nm, but only the resulting photolysis frequencies for a few species were reported, including in particular NO$_2$ and O$_3$→O(^1D). In order to calculate other photolysis frequencies we use a six-stream radiative transfer model for the Rayleigh scattering atmosphere [*Logan et al.*, 1981]. The ozone column was obtained from TOMS satellite data corresponding to the day of the measurements and interpolated along the flight track. Clear skies and a ground albedo of 0.1 were assumed. The model-calculated photolysis frequencies for NO$_2$ and O$_3$→O(^1D), J(NO$_2$) and J(O^1D), were compared to observations, and the difference was attributed to cloud effects [*Schultz et al.*, 1999]. Photolysis frequencies for other species were then calculated by applying the J(O^1D) cloud scaling factor to wavelengths less than 330 nm and the J(NO$_2$) scaling factor to higher wavelengths. During SONEX the average cloud scaling factors for J(NO$_2$) and J(O^1D) were 1.00 ± 0.13 and 1.08 ± 0.15, respectively. When actinic flux measurements were not available, clear-sky model calculations were used.

In addition to local calculations of OH and HO$_2$ concentrations, the diel steady state model is also used to infer 24-hour average production and loss rates for HO$_x$ species. Instantaneous production and loss rates are first calculated along the flight tracks by using local observations and the model chemical mechanism. Species which are not measured such as NO$_2$, HNO$_4$, O(^1D), and CH$_3$O$_2$ are computed from the model. The instantaneous rates are then scaled by a model-derived diel factor to obtain 24-hour average values:

$$<Rate_{obs}>_{24h} = Rate_{obs}(t) \times <Rate_{model}>_{24h}/Rate_{model}(t) \quad (1)$$

where $<Rate_{obs}>_{24h}$, $Rate_{obs}(t)$, $<Rate_{model}>_{24h}$, $Rate_{model}(t)$ represent observed and model-calculated instantaneous and 24-hour average rates.

4. Comparison Between Observed and Modeled HO$_x$

Figure 2 compares observed and modeled HO$_x$ concentrations for the 13 SONEX flights during which OH and HO$_2$ were measured in the 8-12 km altitude range. The model results were obtained with our "standard" diel steady state model which is constrained with observed H$_2$O$_2$, CH$_3$OOH (when above LOD), O$_3$, NO, H$_2$O, PAN, HNO$_3$, CO, CH$_4$, ethane, propane, C$_4$ alkanes, acetone, temperature, pressure, aerosol surface area, and actinic fluxes (see previous section). Formaldehyde was computed at chemical steady state in the model. For 55% of the points shown in Figure 2, model and observations agree within the 40% stated accuracy of the measurements (shown by the dashed lines). The median ratio of model-to-observed HO$_2$, R_{HO2} = [HO$_2$]$_{model}$/[HO$_2$]$_{obs}$, is 1.02. Large discrepancies are noted for the lowest mixing ratios of HO$_2$ (<0.8 pptv), where the model underestimates observations by factors of 2-5, as well as for the largest mixing ratios of HO$_2$ (>3 pptv), where the model overestimates the observations by factors of 1.2-2. Most of the underestimates correspond to observations made at high solar zenith angles (SZA>80°). These observations close to

sunrise and sunset are marked by open circles in Figure 2. Many of the overestimates correspond to observations inside cirrus clouds, marked by plusses in Figure 2. When segregated according to SZA and occurrence of cirrus clouds, we find that R_{HO2} = 0.28 for SZA>80°, R_{HO2} = 1.34 inside cirrus clouds, and R_{HO2} = 1.12 for the remainder of the data (SZA<80°, outside cirrus clouds). Similar conclusions are drawn for the comparison between the observed and model-calculated OH concentrations (lower panel of Figure 2).
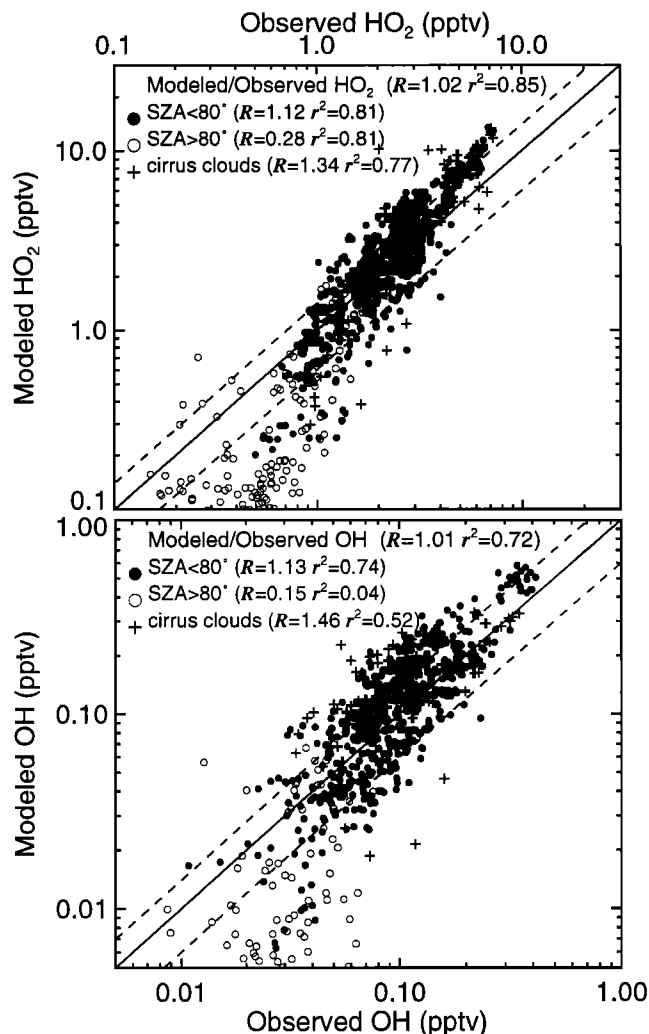

Figure 2. Comparison between observations and model calculations for HO$_2$ and OH mixing ratios during SONEX between 8 and 12 km. The calculations were made with a diel steady state model constrained with observed H$_2$O$_2$, CH$_3$OOH (when above LOD), O$_3$, NO, H$_2$O, PAN, HNO$_3$, CO, CH$_4$, ethane, propane, C$_4$ alkanes, acetone, and actinic fluxes at the time of observations ("standard" model). Model inputs are averaged over the peroxides measurement interval. The open circles correspond to observations made close to sunrise or sunset (solar zenith angle>80°). The plusses indicate observations inside cirrus clouds, and the remaining observations are shown by solid circles. The median ratios (R = [HO$_2$]$_{model}$/[HO$_2$]$_{obs}$ or R = [OH]$_{model}$/[OH]$_{obs}$) and the correlation coefficients r^2 are listed in the legend. The dashed lines correspond to the ±40% accuracy of the observations, while the 1:1 line is indicated by the solid line.
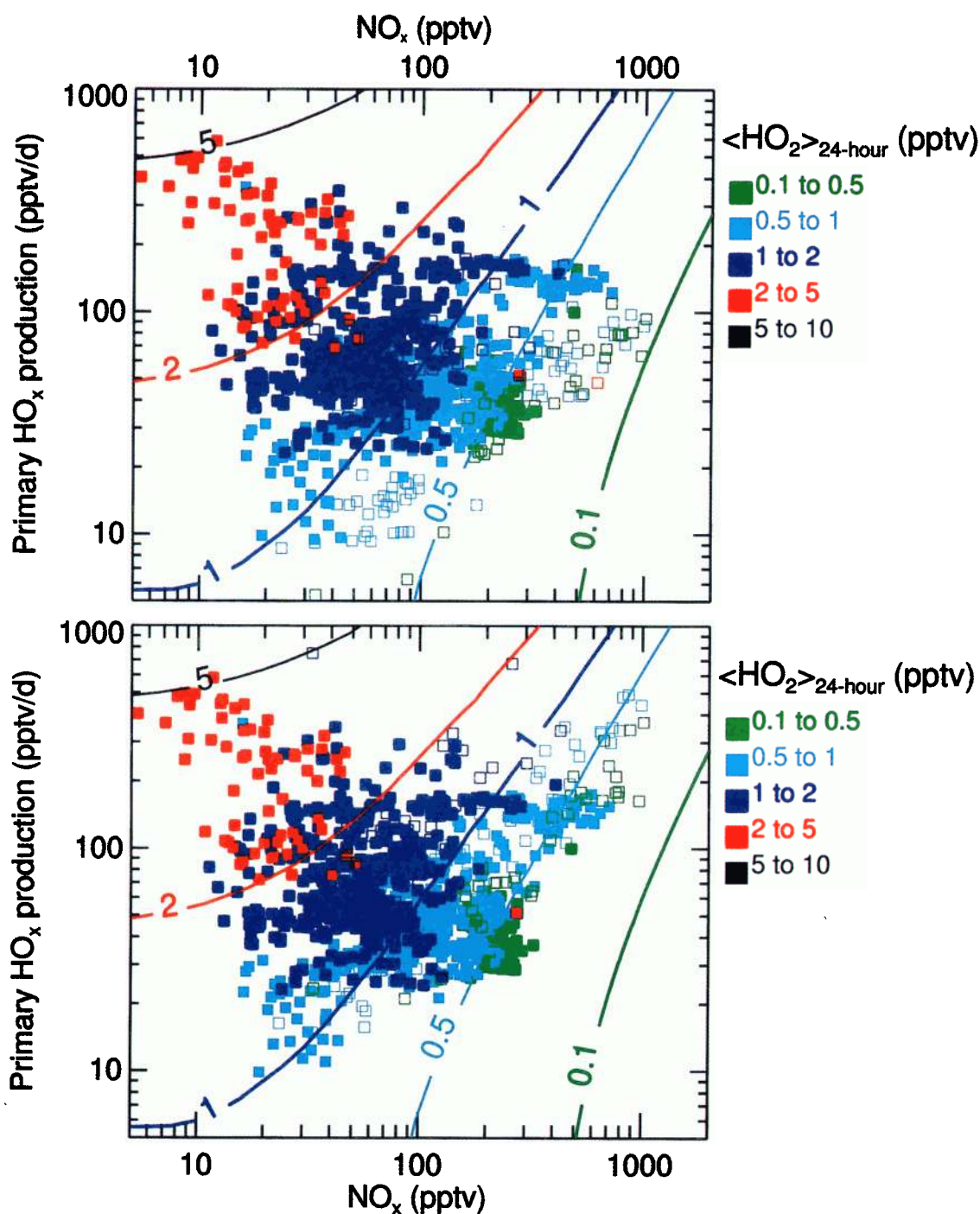
Plate 1. Dependence of HO$_2$ concentrations on NO$_x$ concentrations and the primary HO$_x$ source in the upper troposphere (8-12 km) during SONEX. All values are 24-hour averages. The contour lines correspond to model calculations of HO$_2$ for median background conditions (Table 2). The observed HO$_2$ mixing ratios, scaled by a model-calculated diel factor, are shown as color-coded squares. Observations with stratospheric influence, inside clouds and outside of daytime have been excluded from this Plate. In the upper panel the values of P(HO$_x$) corresponding to the observed HO$_2$ (squares) are calculated from the observed concentrations of H$_2$O and acetone. In the lower panel we adjusted P(HO$_x$) to match the observations of HO$_x$ (see text). The points for which P(HO$_x$) had to be adjusted by more than a factor of 1.5, are singled out by open squares in both panels.

If we were to relax the constraints on our "standard" model calculation and calculate H_2O_2 and CH_3OOH to be in diel steady state (as opposed to using observed values where above LOD), the resulting calculated HO_2 would be very close to the results shown in Figure 2: $R_{HO2} = 1.05$ (compared to 1.02 in top panel of Figure 2). Only in 20% of the cases are differences between the two calculations larger than 20%. This illustrates the relatively minor role of peroxides as a net source of HO$_X$ during SONEX (see section 6).

Brune et al. [1999] present comparisons of the observed and modeled OH/HO_2 concentration ratios, diagnosing the fast chemical cycle between OH and HO_2. Agreement to within 20% is found for the ensemble of SONEX observations at 8-12 km altitude. The cycle is driven primarily by the reactions $OH+CO$, HO_2+NO and HO_2+O_3.

Figure 3 shows the same comparison for HO_2 as Figure 2 but using observed CH_2O concentrations to constrain the model. The calculations are only shown for the subset of 45 points where the peroxides and CH_2O were above their respective LOD. The model inputs are averaged over the CH_2O measurement interval. For reference, model calculations where CH_2O is calculated instead of being specified from observations are shown on the bottom panel for the same subset of points. We find that the model constrained with observed CH_2O overestimates HO_2 concentrations by a factor of 1.6 (top panel of Figure 2), compared to a factor of 1.3 when we use calculated CH_2O instead (bottom panel of Figure 3). As will be discussed in section 6, CH_2O observations above their LOD were often much larger than expected from diel steady state calculations. These high values of CH_2O when used to constrain the model result in an additional HO$_X$ source. Given the limited number of points, and the accuracy of the HO_2 and CH_2O measurement (Table 1), it is difficult to draw general conclusions as to whether CH_2O observations are inconsistent with observed HO_2.

For the rest of this analysis we consider only the "standard" model calculation where CH_2O is assumed to be at chemical steady state (Figure 2). We first examine the factors controlling the variance of HO$_X$ for the cases where the model successfully reproduces the observations (SZA<80°, outside cirrus clouds). We then focus on explaining the discrepancies at sunrise and sunset (SZA>80°) and inside cirrus clouds.

4.1. Variance of HO$_X$ Concentrations

Our model reproduces 85% of the observed variance of HO_2 concentrations during SONEX (Figure 2). For OH this fraction is somewhat lower (72%), due to additional noise in the observations. The variance in the HO_2 observations for SZA<80° is mostly driven by changes in SZA ($r^2 = 0.40$), concentrations of NO_x ($r^2 = 0.15$), and water vapor ($r^2 = 0.20$).

We have shown before [*Jaeglé et al.*, 1998] that, once the obvious dependence on SZA is eliminated, the variability of HO_2 concentrations in the upper troposphere can be largely accounted for by two independent variables: (1) the primary HO$_X$ source and (2) the concentration of NO_x. This relationship is shown in Plate 1 for the SONEX data. In the upper panel of Plate 1 we calculate the primary HO$_X$ source, $P(HO_x)$, based on 1-min averages of observed H_2O and acetone concentrations. The sources from $O(^1D)+H_2O$ and acetone photolysis are averaged over 24 hours and weighted by their respective primary yields in HO$_X$. The contour lines in Plate 1 correspond to model calculations of HO_2 for the median background air conditions during SONEX (Table 2) with variable NO_x and $P(HO_x)$, and for November 1 (45°N latitude; 10 km altitude). The observed HO_2 mixing ratios, converted to 24-hour average values using a model diel factor, are shown by the squares.

For 15% of the cases shown in Plate 1 and Figure 2 (SZA<80°, outside cirrus) the model underestimates the HO_2 observations by more than 40%. These observations are generally associated with high levels of NO_x (>200 pptv) from convection and lightning [*Jaeglé et al.*, 1999]. These higher than expected levels of HO$_X$ could be due to the presence of unmeasured sources, such as higher aldehydes, possibly also resulting from convection [*Müller and Brasseur*, 1999], or alternatively they could reflect flaws in our understanding of
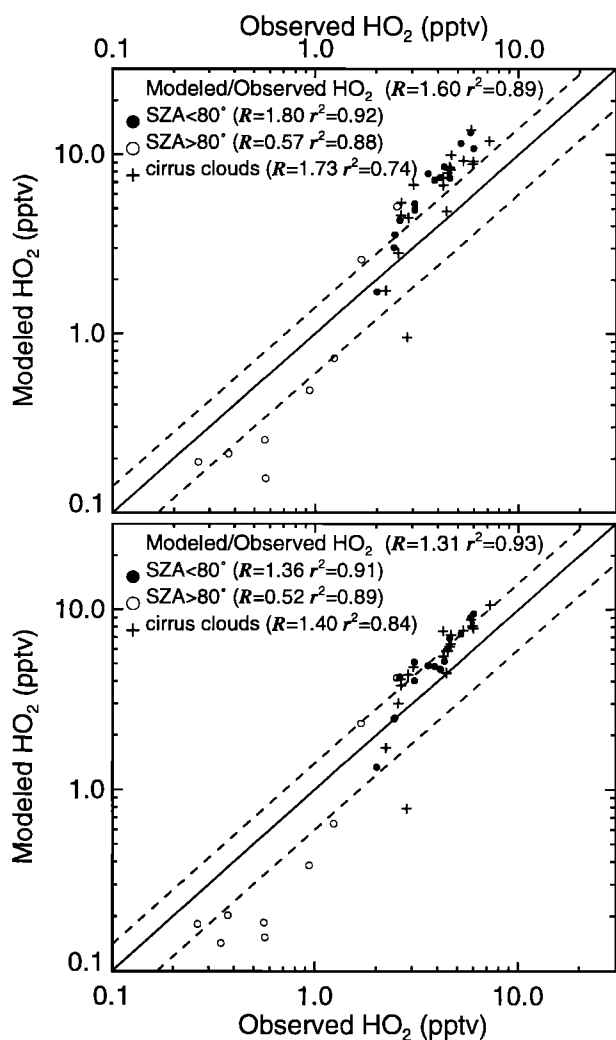

Figure 3. Comparison between observations and model calculations for HO_2 mixing ratios during SONEX at 8-12 km altitude. The model calculations on the top panel were obtained using a diel steady state model constrained with observed CH_2O, in addition to all the other parameters. Model inputs are averaged over the CH_2O measurement interval. The lower panel shows the standard model calculations for the same points, with CH_2O calculated from chemical steady state instead of being specified from observations.

HO$_x$ chemistry under high NO$_x$ conditions [*Brune et al.*, 1999; *Faloona et al.*, this issue]. These points have been singled out by open symbols in Plate 1. In the lower panel of Plate 1, in addition to H$_2$O and acetone, we include supplementary primary HO$_x$ sources as required to match the observed HO$_2$ concentrations indicated by open squares.

Plate 1 shows the rapid decrease of HO$_2$ with increasing NO$_x$ both in the observations and in the model. As NO increases, the OH/HO$_2$ ratio increases due to the HO$_2$+NO reaction. This leads to faster loss of HO$_x$ through the reactions of OH with HO$_2$ or with HNO$_4$ (see section 5), and hence a decrease of HO$_2$. Plate 1 also illustrates the increase in the concentration of HO$_2$ with increasing P(HO$_x$). The high values of P(HO$_x$) (200-700 pptv/d) associated with low NO$_x$ concentrations (<60 pptv) in Plate 1 correspond to air masses influenced by recent marine convection and are characterized

by high levels of CH$_3$I, H$_2$O$_2$, CH$_3$OOH, and H$_2$O (Table 2). The combination of low NO$_x$ and elevated P(HO$_x$) results in the highest observed levels of HO$_2$.

4.2. Sunrise and Sunset

Sunrise observations made during a transit flight between the Azores and Maine on October 31 are shown in Figure 4 as a function of solar time. Sunrise was at 0654 LT as the DC-8 was flying at an altitude of 9 km. During the first hour after sunrise, the observations of HO$_2$ indicate mixing ratios close to 0.5 pptv, while the standard model predicts only 0.1-0.2 pptv of HO$_2$ (bottom panel of Figure 4). The measurement of 0.5 pptv HO$_2$ at sunrise is 4 times above the detection limit of the instrument (Table 1). At such high SZA the HO$_x$ sources from O(^{1}D)+H$_2$O and acetone photolysis are extremely slow; peroxides and CH$_2$O are the dominant sources of HO$_x$ in the standard model. The discrepancy with observations clearly points to a missing source of HO$_x$.

Heterogeneous conversion of NO$_2$ to HONO at night followed by photolysis of HONO at sunrise is known to be an important early morning source of HO$_x$ in urban air [*Jenkin et al.*, 1988]. Laboratory measurements suggest that NO$_2$ disproportionation to HONO and HNO$_3$ on aqueous aerosols can be parameterized by a reaction probability $\gamma_{NO2}= 10^{-4}$-10^{-3} [*Jacob*, 1999]:

(R2) NO$_2$ + aerosol (+ ½ H$_2$O) → ½ HONO + ½ HNO$_3$.
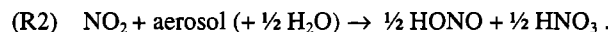
Results for a model simulation including reaction (R2) with $\gamma_{NO2} = 10^{-3}$ are shown in the bottom panel of Figure 4 (solid line). The observed aerosol surface areas varied between 10 and 60 μm^2 cm^{-3} for this flight. As a result of (R2), between 5 and 10 pptv of HONO are produced during the night (second panel in Figure 4, dotted line). The photolysis of HONO produced through reaction (R2) is a strong enough source of HO$_x$ at sunrise to account for the observed concentrations of HO$_2$ after 0730 LT. Before that time, the source from (R2) seems insufficient to explain the observed HO$_2$. After 0900 LT (74° SZA), most of the HONO produced at night has photolyzed, and the dominant primary sources of HO$_x$ are O(^{1}D)+H$_2$O and acetone photolysis.

We had previously proposed, in the context of OH and HO$_2$ observations in the tropical upper troposphere, a large sunrise source of HO$_x$ from the photolysis of convected peroxides [*Jaeglé et al.*, 1997]. For the SONEX flight shown in Figure 4, high concentrations of CH$_3$I and CH$_3$OOH (0.3-0.5 pptv and 50-130 pptv respectively) were observed until 0730 LT, indicating a recent convective origin of the air for this early part of the flight. Concentrations of CH$_2$O were not measured. It is possible that the unmeasured CH$_2$O could explain the elevated concentrations of HO$_2$ before 0730 LT, which cannot be accounted for by photolysis of HONO. We calculate that 200-300 pptv of CH$_2$O would be necessary to explain the observed HO$_2$ between 0700 and 0730 LT. Such elevated concentrations have been observed during SONEX.

An alternative explanation for these sunrise observations of HO$_2$ is a source of HO$_x$ through the photolysis of HNO$_4$ at long wavelength (650-1250 nm) [*Wennberg et al.*, 1999]. The existence of a HNO$_4$ photolysis integrated band cross section of 2.5×10^{-20} cm^2 molecule^{-1} nm in the red/near-IR, as speculated by *Wennberg et al.* [1999], would match the required sunrise source to account for the observed HO$_2$ in Figure 4 between 0700 and 0900 LT.
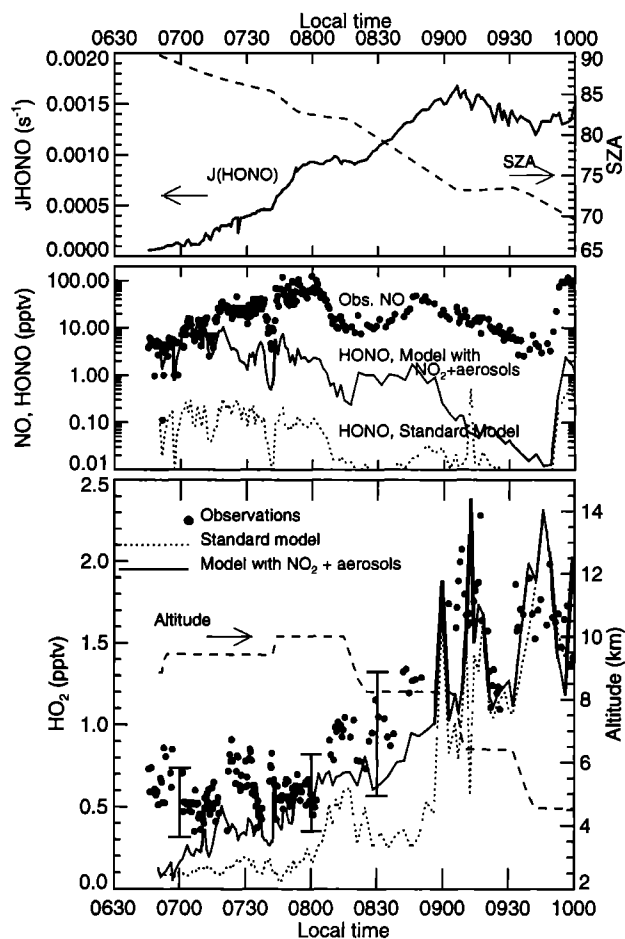

Figure 4. SONEX flight of October 31, 1997: transit flight between the Azores and Maine. Observations of the HONO photolysis frequency, NO, and HO$_2$ are shown as a function of solar time. Sunrise occurred at 0654 LT as the aircraft was flying at an altitude of 9 km. The bottom panel compares the observed HO$_2$ (solid circles) and diel steady state model calculations with (solid line) and without (dotted line) heterogeneous reaction NO$_2$ + aerosol → ½HONO + ½HNO$_3$ ($\gamma_{NO2} = 10^{-3}$). The solar zenith angle and the aircraft altitude are shown on the top and bottom panels, respectively (dashed lines). The error bars indicate the 40% accuracy of the HO$_2$ measurement.

Observations at sunset during SONEX are more difficult to interpret. For some flights (October 13 and 18), model and observations agree for SZA>80°, while for some others (October 15 and November 9) the model is a factor of 3-5 too low, and for one flight (October 28), the model overestimates the observations by up to 60%. The behavior of HO$_2$ at high SZA is very sensitive to the kinetics of HNO$_4$. Poorly known rates for HNO$_4$ formation and loss could be another explanation for these discrepancies between model and observations at sunrise and sunset [Brune et al., 1999].

4.3. Cirrus Clouds

During a southern flight out of Ireland on October 20, 1997, the DC-8 flew in the vicinity of outflows from developed convective cells, and clouds were present at all
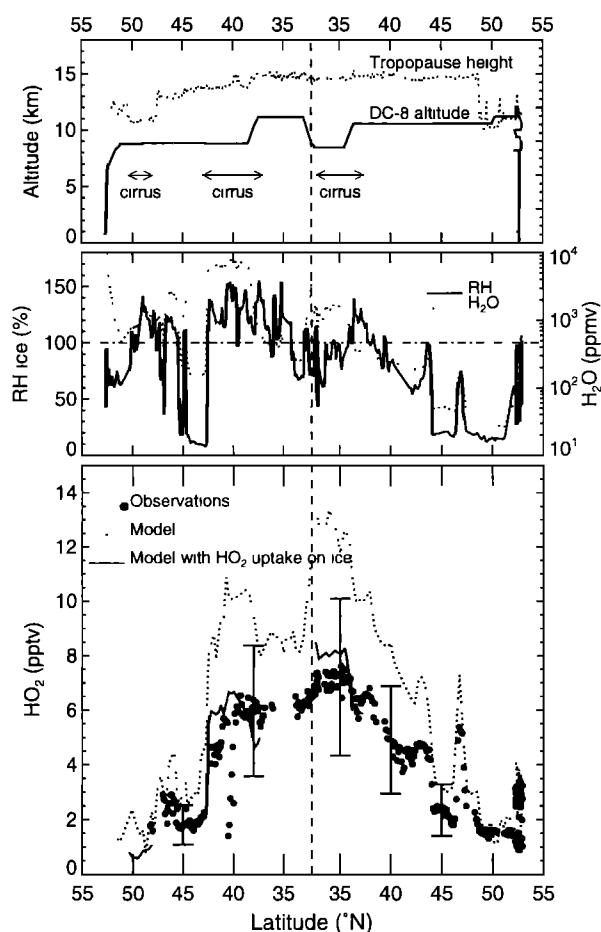

Figure 5. SONEX flight of October 20, 1997: southern survey from Ireland (52°N) to 32°N. Altitude, relative humidity over ice, H$_2$O, and HO$_2$ are shown as a function of latitude on the southbound and northbound flight legs. Arrows on the top panel indicate the occurrence of cirrus, based on the presence of supermicron particles (3-24 μm). Two diel steady state model calculations are shown on the bottom panel. The dotted line represents the standard model, while the solid line includes uptake of HO$_2$ on the surface of cirrus clouds assuming a surface area of 500 μm^2 cm^{-3} and γ_{ice_HO2} = 0.025. The observed tropopause height is indicated by the dotted line on the top panel. The error bars show the 40% accuracy of the HO$_2$ measurement.

levels. Observations of HO$_2$, water vapor, and relative humidity over ice are shown in Figure 5 from 53°N to 32°N on the southbound and northbound flight legs. The DC-8 flew through extended cirrus clouds fields for long periods of time on three occasions. North of 43°N the observed HO$_2$ was about 2 pptv, and the diel steady state model is within 10-40% of observations. South of 43°N the observed HO$_2$ increased to 6-7 pptv, reflecting the increase in water vapor, and the model predicts 1.5-2 times more HO$_2$ than observed. The overestimate is particularly large inside the cirrus clouds but extends to portions of the flights when the DC-8 was not inside clouds. On the return leg a low tropopause allowed the DC-8 to sample dry stratospheric air with ozone levels of up to 120 ppbv at 49°-53°N. There is good agreement between model and observations for this part of the flight.

Previous aircraft observations of depleted concentrations of HO$_2$ inside cirrus clouds [Faloona et al., 1998] have pointed to the possible role of ice crystals as sinks of HO$_x$. In the laboratory, Cooper and Abbatt [1996] measured a reactive uptake coefficient of 0.025 for HO$_2$ on ice at 223 K. The observed first-order loss of HO$_2$ was independent of the exposure time of the ice surface to HO$_2$, suggesting an irreversible loss not limited by the number of active sites available on the ice. We include in the model reactive uptake of HO$_2$ on ice (γ_{ice_HO2} = 0.025), and estimate the ice surface area required to account for the observations of HO$_2$ inside the cirrus clouds. We find that an ice surface of 500 μm^2/cm^3 affords a good match between calculated and observed HO$_2$ (Figure 5). Observations of cirrus clouds over the central United States show surface areas between 50 and 2000 μm^2/cm^3 [Gerber et al., 1998]. It is thus possible that the discrepancy between model and observations inside cirrus clouds could be due to HO$_2$ reactive uptake on the ice particles. Given a 10-15 min lifetime for HO$_x$ outside of clouds and typical wind speeds of 20-40 m/s, it is then possible that depressed HO$_x$ could be observed up to 20 km downstream of cirrus after the ice particles evaporate. Parts of the southbound flight leg (50°-47°N and 37°-32°N) and the northbound flight leg (37°-45°N) show relative humidities close to 100% and could thus have been influenced by recently evaporated cirrus clouds.

On the other occasions when the DC-8 was flying inside cirrus clouds (October 28 and October 25), the model also overestimates the observations by up to a factor of 2. Inclusion of HO$_2$ uptake on ice crystals brings model and observations in better agreement.

5. Sources and Sinks of HO$_x$ and HO$_y$

We now examine the sources and sinks of HO$_x$ and of the larger family HO$_y$ for SZA<80° and outside of cirrus clouds at 8-12 km. Table 3 shows median HO$_x$ and HO$_y$ production and loss rates inferred from observations (see section 3) for 40°-60°N latitude. Observations with stratospheric influence are not included in this table. The fairly good agreement between the total HO$_x$ production rate (146 pptv/d) and loss rate (117 pptv/d) reflects the ability of the model to simulate well the observed HO$_x$ concentrations, with a tendency to overestimate the observations by 10-20% (Figure 2).

5.1. Sources of HO$_x$ and HO$_y$

The median sources of HO$_x$ from O(^{1}D)+H$_2$O and acetone photolysis were of 25 and 14 pptv/d, respectively. The HO$_x$

Table 3. Median Production and Loss Rates for HO$_x$, HO$_y$, and Associated Species in the Upper Troposphere During SONEX (8-12 km; 40°-60°N)

	Sources	24-hour rates, pptv/d	Sinks	24-hour rates, pptv/d
HO$_x$	CH$_2$O + $h\nu$	45.3	HO$_2$ + NO$_2$ + M	29
1.2 pptv [a]	O(^{1}D) + H$_2$O	24.7	OH + HO$_2$	17.8
	H$_2$O$_2$ + $h\nu$	16.5	HO$_2$ + HO$_2$	14.5
	acetone + $h\nu$	14	OH + HNO$_4$	12.1
	HNO$_4$ + M	7.6	[b] HO$_2$ + aerosol	10
	HNO$_4$ + $h\nu$	7	OH + NO$_2$ + M	7.8
	CH$_3$OOH + $h\nu$	4.5	HO$_2$ + CH$_3$O$_2$	7.4
	HNO$_3$ + $h\nu$	0.8	OH + HNO$_3$	1.1
	Total production	146	Total loss	117
			Lifetime	15 min
HO$_y$	CH$_2$O + $h\nu$	45.3	OH + HNO$_4$	24.1
246 pptv [a]	O(^{1}D) + H$_2$O	24.7	OH + HO$_2$	17.8
	acetone + $h\nu$	14	OH + NO$_2$ + M	7.8
	HNO$_3$ + $h\nu$	0.8	OH + CH$_3$OOH	6
			OH + H$_2$O$_2$	4.5
			OH + HNO$_3$	1.1
	Total production	92	Total loss	69
			Lifetime	3.5 days
H$_2$O$_2$	HO$_2$ + HO$_2$	7.2	H$_2$O$_2$ + $h\nu$	8.7
66 pptv	[b] HO$_2$ + aerosol	5	OH + H$_2$O$_2$	2.3
	Total production	14	Total loss	11.1
			Lifetime	5.2 days
CH$_3$OOH [c]	HO$_2$ + CH$_3$O$_2$	7	OH + CH$_3$OOH	10
58 pptv			CH$_3$OOH + $h\nu$	8.8
	Total production	7	Total loss	18.7
	Number of observations	114	Lifetime	3.4 days
CH$_3$O$_2$	OH + CH$_4$	46	CH$_3$O$_2$ + NO	76.1
0.3 pptv [a]	acetone + $h\nu$	14	HO$_2$ + CH$_3$O$_2$	3.5
	OH + CH$_3$OOH	2.2		
	Total production	65	Total loss	81
			Lifetime	5 min
CH$_2$O [c]	CH$_3$O$_2$ + NO	82	CH$_2$O + $h\nu$ → H$_2$ + CO	127
80 pptv	CH$_3$OH + OH	5	CH$_2$O + $h\nu$ → H + HCO	60
	OH + CH$_3$OOH	2	CH$_2$O + OH	21
	Total production	92	Total loss	208
	Number of observations	22	Lifetime	12 hours

We use the following definitions for HO$_x$ and HO$_y$: HO$_x$ = OH + HO$_2$ + H + RO$_2$, and HO$_y$ = HO$_x$ + 2 H$_2$O$_2$ + 2 CH$_3$OOH + HNO$_2$+ HNO$_4$. Observations with stratospheric influence, inside cirrus clouds, and for SZA>80° have been excluded from this table. Concentrations of NO$_2$, HNO$_4$, CH$_3$O$_2$, CH$_2$O, and O(^{1}D) are model-calculated values. All the other concentrations are based on observations, using the model-computed diel cycles to convert instantaneous rates to rates averaged over 24 hours (equation 1). Because the values shown are medians, the sum of individual rates does not usually match the given total production or loss rates.

[a] The 24-hour average concentrations are calculated using the model-computed diel cycles.

[b] The assumed reaction probability for the heterogeneous reaction of HO$_2$ on aerosols is γ_{HO2}=0.2.

[c] For the CH$_3$OOH and CH$_2$O budgets, median values for the subset of measurements above the detection limit (25 pptv for CH$_3$OOH, 50 pptv for CH$_2$O) are reported. The median for the complete data set was below the detection limit for both CH$_3$OOH and CH$_2$O (see Table 2).

source from acetone listed in Table 3 includes only the direct source, that is, two HO$_x$ molecules produced for each acetone photolyzed. Including the supplemental source of HO$_x$ by photolysis of CH$_2$O produced from acetone increases the overall HO$_x$ yield to about 3 and results in a total primary HO$_x$ source from acetone of 21 pptv/d, comparable to the source

from O(^{1}D)+H$_2$O. For water vapor concentrations below 100 ppmv, acetone photolysis is usually the dominant source of HO$_x$.

Photolysis of CH$_2$O contributed a median HO$_x$ source of 45 pptv/d, of which 32 pptv/d was due to CH$_2$O produced by methane oxidation. Methane oxidation thus amplifies the

primary HO$_x$ source by a median factor of 1.7 [Logan et al., 1981].

The peroxides contributed about 21 pptv/d of HO$_x$, about half the primary HO$_x$ source from acetone and water vapor, with photolysis of H$_2$O$_2$ being more important than photolysis of CH$_3$OOH. These sources were, however, balanced by a 22 pptv/d sink of HO$_x$ through the formation of peroxides (HO$_2$+HO$_2$ and HO$_2$+CH$_3$O$_2$), thus not representing a net source of HO$_x$ (Table 3). Previous observations at 11-14 km in tropical convective outflows showed a much more pronounced role of convected peroxides [Jaeglé et al., 1997; Wennberg et al., 1998], enhancing the primary HO$_x$ source by factors of 3-5. Compared to northern midlatitudes in the fall, the more vigorous tropical convection results in the peroxides being injected at higher altitudes in a drier environment (H$_2$O<50 ppmv), thus enhancing their relative impact on HO$_x$ [Prather and Jacob, 1997].

5.2. Sinks of HO$_x$ and HO$_y$

We find that loss of HO$_x$ is dominated by the reactions OH+HNO$_4$ and OH+HO$_2$ (Table 3). Reactions OH+NO$_2$+M, OH+CH$_3$OOH, and OH+H$_2$O$_2$ play smaller roles. Plate 2 shows the relative importance of these different loss pathways as a function of NO$_x$. The lines in this Plate show the dependence of the HO$_y$ loss pathways on NO$_x$ as calculated from the diel steady state model for median background conditions during SONEX (Table 2). Peroxides are at chemical steady state in this calculation. Three chemical regimes can be defined based on the levels of NO$_x$: (1) the NO$_x$-limited regime, (2) a transition regime, and (3) the NO$_x$-saturated regime. Under low NO$_x$ conditions, reactions OH+HO$_2$, OH+H$_2$O$_2$, and OH+CH$_3$OOH are the principal loss pathways (NO$_x$-limited regime). As NO$_x$ increases, HO$_2$ decreases (Plate 1), while HNO$_4$ increases, resulting in a dominant sink from the reaction OH+HNO$_4$ in the 50-400 pptv NO$_x$ range (transition between NO$_x$-limited and NO$_x$-saturated regimes). At higher NO$_x$ concentrations (>500 pptv) one would expect OH+NO$_2$+M to dominate the loss of HO$_y$, because of further decreases in the concentrations of HO$_2$ which slow the formation of HNO$_4$ (NO$_x$-saturated regime). Such conditions were rarely encountered in SONEX, but can be important when NO$_x$ levels are very elevated. The model dependencies of HO$_y$ sinks on NO$_x$ generally follow the relationships found in the observations, but the model underestimates CH$_3$OOH concentrations (see section 6) and hence the role of the OH+CH$_3$OOH reaction as a sink for HO$_y$ under low NO$_x$ conditions. Because loss of HO$_y$ determines the dependence of ozone production, P(O$_3$), on NO$_x$, these three regimes also define the well-known dependence of ozone production on NO$_x$: in the NO$_x$-limited regime, P(O$_3$) increases with increasing NO$_x$, in the transition regime, P(O$_3$) is independent of NO$_x$, and in the NO$_x$-saturated regime (generally referred to as the hydrocarbon-limited regime in the context of the lower troposphere), P(O$_3$) decreases with further increases in NO$_x$ [Jaeglé et al., 1998, 1999].

Reaction OH+HNO$_4$ contributes to one third of the total HO$_y$ loss for median conditions during SONEX and dominates for the high-NO$_x$ regime (>50 pptv). In contrast, it was found to be of minor importance in model analyses of previous aircraft campaigns [Jaeglé et al., 1997; Wennberg et al., 1998; Brune et al., 1998]. The predominant HO$_y$ loss during these campaigns was OH+HO$_2$. For a given level of NO$_x$, the ratio of the rates for OH+HNO$_4$ and OH+HO$_2$ is

roughly proportional to the concentration of NO$_2$. The importance of OH+HNO$_4$ during SONEX reflects the weak photochemical environment (northern midlatitudes fall) and hence the high NO$_2$/NO$_x$ ratio. Folkins et al. [1997] also pointed to the dominant role of OH+HNO$_4$ as a sink of HO$_y$ in one of the cases they examined at southern midlatitudes during austral fall. The dominance of the OH+HNO$_4$ loss pathway (transition region between NO$_x$-limited and NO$_x$-saturated regimes) implies little dependence of ozone production on NO$_x$ during SONEX [Jaeglé et al., 1999].

6. Peroxides and Formaldehyde

We now examine the production and loss rates of H$_2$O$_2$, CH$_3$OOH, and CH$_2$O as constrained by the ensemble of observations on board the aircraft including OH, HO$_2$, CH$_4$, acetone, NO, and photolysis frequencies (Table 3). Given the relatively short lifetimes of peroxides (5 days for H$_2$O$_2$ and 3 days for CH$_3$OOH) and CH$_2$O (12 hours) in the upper troposphere, we expect their production and loss rates to be roughly in balance, except in recently convected air masses.

6.1. Hydrogen Peroxide

The computed production and loss rates for H$_2$O$_2$ in Table 3 are in fairly close balance. Loss of H$_2$O$_2$ (median 11 pptv/d) is dominated by photolysis. Production of H$_2$O$_2$ based on self-reaction of HO$_2$ is 7.2 pptv/d. In our standard model we have included an additional source of H$_2$O$_2$ through the heterogeneous reaction of HO$_2$ on aerosols with γ_{HO2} = 0.2 (reaction (R1)). This reaction is generally not included in atmospheric models, but we find in SONEX that it is an important source of H$_2$O$_2$, comparable to the gas-phase source (Table 3). Figure 6 compares observed H$_2$O$_2$ concentrations to chemical steady state values computed with the standard model (top panel) and a model with γ_{HO2} = 0 (bottom panel). Including heterogeneous production of H$_2$O$_2$ improves the agreement between observed and calculated H$_2$O$_2$ by almost a factor of 2. While being a strong source of H$_2$O$_2$, reaction (R1) has little effect on HO$_2$ concentrations because it is generally not the dominant HO$_x$ sink in the upper troposphere (it represents 10% of the total HO$_x$ loss, Table 3). Accounting for the conversion of HO$_2$ to H$_2$O$_2$ in aerosols could possibly resolve previous model underestimates of H$_2$O$_2$ concentrations measured from aircraft above 8 km altitude [Jacob et al., 1996; Schultz et al., 1999; Crawford et al., 1999].

For air masses affected by recent convection, inclusion of reaction (R1) also results in a near balance between production and loss of hydrogen peroxide (not shown). Elevated concentrations of H$_2$O$_2$ in tropical and midlatitude marine convection are maintained by high concentrations of HO$_2$ (Table 2), which are themselves due to enhancements in water vapor (and of CH$_3$OOH to a lesser extent). Cycling of HO$_y$ can maintain elevated H$_2$O$_2$ in a convective outflow for several days following the convective event [Cohan et al., 1999; Jaeglé et al., 1997].

6.2. Methylhydroperoxide

Figure 7 shows the frequency distribution of the ratio of chemical loss L to chemical production P of CH$_3$OOH for the different air mass categories in Table 2. Only data points where CH$_3$OOH was above the LOD of 25 pptv are included in this figure. There is a systematic imbalance between
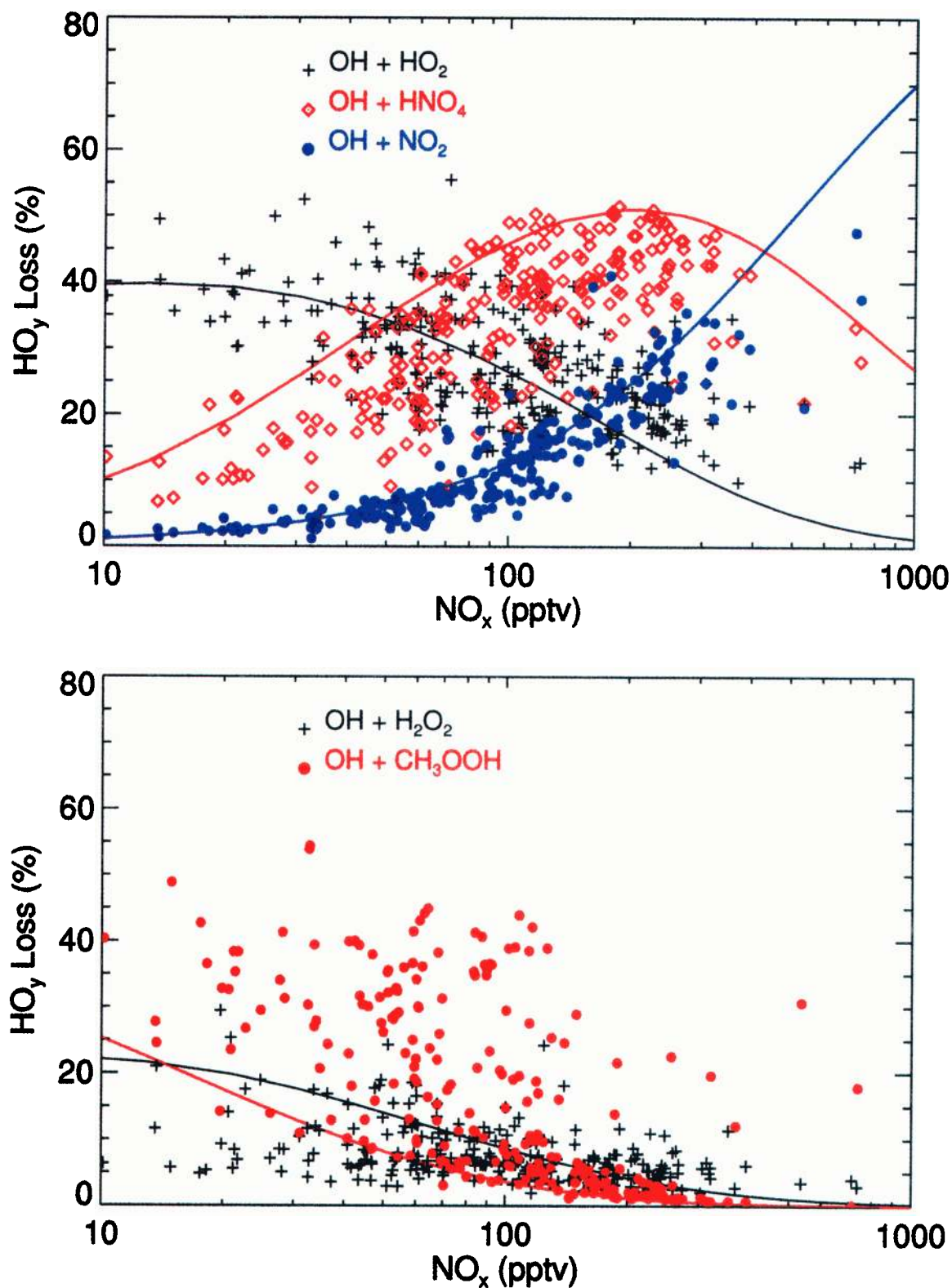
Plate 2. Relative importance of different HO_y sinks as a function of NO_x mixing ratios in the upper troposphere (8-12 km altitude) during SONEX. The upper panel shows the relative contributions from $OH+HO_2$ (black plusses), $OH+HNO_4$ (red diamonds), and $OH+NO_2$ (blue circles), while the lower panel shows the contributions from $OH+H_2O_2$ (black plusses) and $OH+CH_3OOH$ (red circles). The contribution from $OH+HNO_3$ is small (<1%) and is not shown here. Observations with stratospheric influence, inside cirrus clouds, and SZA>80° are excluded. The lines are model results for median background conditions during SONEX (Table 2).
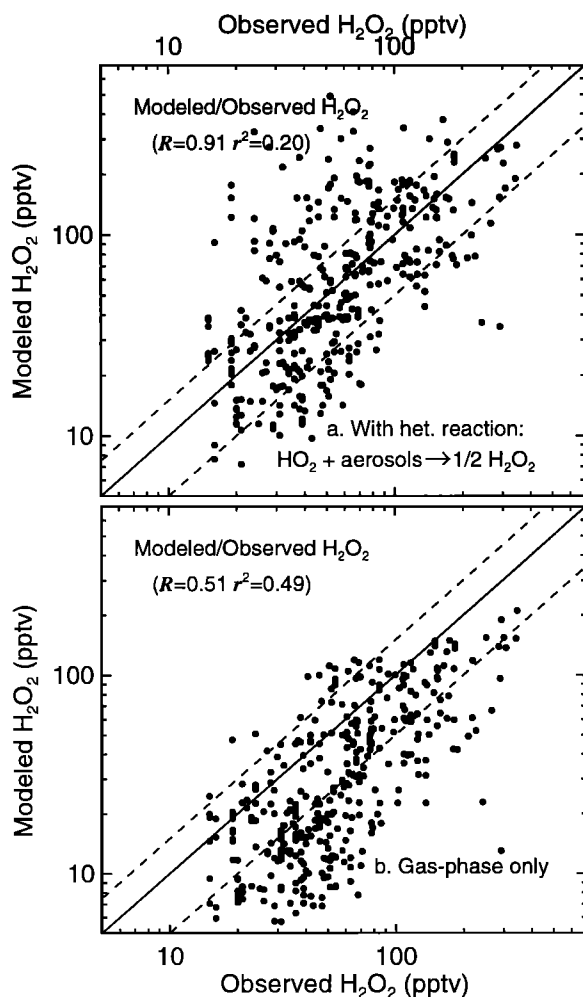
Figure 6. Comparison of observed concentrations of H$_2$O$_2$ with model calculations using the observations of HO$_2$, OH, H$_2$O$_2$ photolysis frequency, temperature, aerosol surface area, and assuming diel steady state. (a) Model results that include the heterogeneous reaction HO$_2$ + aerosol → ½H$_2$O$_2$ (γ_{HO2} = 0.2) and (b) model results with γ_{HO2} = 0. The 1:1 line is indicated, along with the uncertainty on the observed H$_2$O$_2$. The median ratio of model-to-observed H$_2$O$_2$ (R) and the correlation coefficient r^2 are given in the legend.

computed production and loss of CH$_3$OOH across all air masses. Table 3 shows a median imbalance between production and loss of CH$_3$OOH of 2.3 for observations above the LOD: the calculated CH$_3$OOH loss rate exceeds its production rate by factors of 2-15 (Figure 7).

Such imbalances in the CH$_3$OOH budget might be expected as a result of convective influence [*Prather and Jacob*, 1997]. The largest imbalances in Figure 7 are found in outflows of continental convection, but this result likely reflects local suppression of CH$_3$OOH production due to high concentrations of NO. The largest concentrations of CH$_3$OOH were measured in marine convective outflows (Table 2) as would be expected in view of the high CH$_3$OOH concentrations in boundary layer air [*Cohan et al.*, 1999; *Heikes et al.*, 1996]. However, the imbalance between CH$_3$OOH loss and production also extends to air masses not recently affected by convection (background and stratospheric influence). One possible explanation involves the kinetics of

CH$_3$OOH formation. The uncertainty on the rate constant for the HO$_2$+CH$_3$O$_2$ reaction is estimated to be a factor of 3 at 235 K [*DeMore et al.*, 1997]. A factor of 2 increase in this rate constant from the value used in our standard model would largely reconcile our computed chemical production and loss rates of CH$_3$OOH.

6.3. Formaldehyde

The dominant source of CH$_2$O in the upper troposphere during SONEX was methane oxidation, with acetone photolysis contributing about 20% and methanol oxidation about 5% (Table 3). Nonmethane hydrocarbons did not contribute significantly. For the ensemble of points where CH$_2$O was above the detection limit, the sum of all computed sources is less than half the computed sink (Table 3). The discrepancy exceeds the uncertainties in the kinetic parameters of the known reactions for production (±55%) and loss (±50%) of CH$_2$O. There appears to be a large missing source of CH$_2$O.

Close to 55% of the CH$_2$O observations reported during SONEX were below the 50 pptv detection limit of the instrument. Figure 8 shows a comparison between observations of CH$_2$O and diel steady state model calculations using the observed OH, CH$_4$, acetone, CH$_3$OH, CH$_3$OOH, and photolysis rates. For observations below the LOD the median model-calculated CH$_2$O is of 29 pptv, not inconsistent with observations. For observations above the LOD the model is systematically too low by factors of 2-3 and does not capture the observed variability.

Median observed CH$_2$O concentrations are above the LOD only for measurements in continental outflows and in cirrus clouds (Table 2). Convective transport of high levels of CH$_2$O from the surface, especially from polluted boundary layer air [*Müller and Brasseur*, 1999], can enhance upper tropospheric concentrations of CH$_2$O. However, with its short lifetime of 12 hours (Table 3) we would expect CH$_2$O to adjust to chemical steady state within a day after the convective event. We searched for relationships between high observed CH$_2$O and other measured species, and found the best correlation to occur with methanol (Figure 9). *Singh et al.* [this issue] speculate that heterogeneous conversion of CH$_3$OH to CH$_2$O on aerosols could take place. To our knowledge, no laboratory data are available for this reaction. We calculate that the required reactive uptake of CH$_3$OH on aerosols would be γ_{CH3OH} ≈ 0.01. Enhanced CH$_2$O inside clouds (Table 2) also suggests a possible heterogeneous source from reaction on ice surfaces.

7. Conclusions

Observations of OH, HO$_2$, H$_2$O$_2$, CH$_3$OOH, and CH$_2$O collected during the SONEX aircraft mission at 8-12 km altitude over the north Atlantic in October-November 1997 were analyzed in the context of current chemical understanding using a photochemical 0-D model. This suite of aircraft measurements allows a highly constrained examination of the factors controlling the concentrations of HO$_x$ (= OH + peroxy) radicals. Our model calculations successfully reproduce the observed OH and HO$_2$ concentrations within the instrumental accuracy of 40%. Furthermore, the model captures 85% of the observed variance in HO$_x$, which is driven by the local concentration of NO$_x$ and the strength of the primary sources of HO$_x$
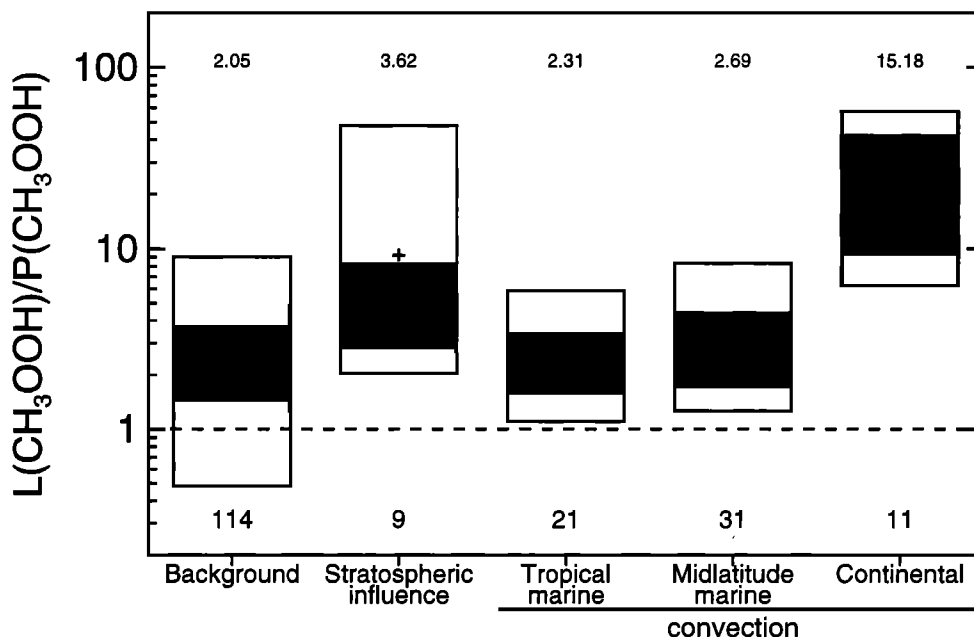
Figure 7. Frequency distribution of the ratio of chemical loss L to chemical production P of CH_3OOH, for different air masses in the upper troposphere (8-12 km) and SZA<80°. The rates are averaged over 24 hours. The means (heavy solid line) and medians (plusses) are indicated along with the central 50% (heavy shading) and central 90%. The median values of the ratios are given on top of each bar, while the number of measurement points within each category is indicated below each bar.
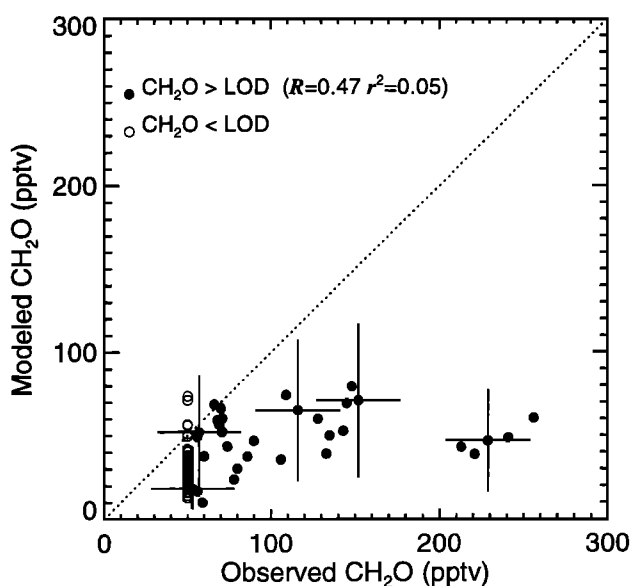

Figure 8. Comparison of observed concentrations of CH_2O with model calculations using the observations of OH, acetone, CH_3OOH, CH_2O photolysis frequency, temperature, and assuming diel steady state for CH_2O. Observations of CH_2O below the LOD (<50 pptv) are shown by open circles, and observations above the LOD are shown by solid circles. The error bars indicate the uncertainties associated with observations and model calculations. The 1:1 line is indicated by the dashed line.

(principally $O(^1D)+H_2O$ and acetone photolysis). The decrease of the observed concentrations of HO_2 with increasing NO_x is as expected from model calculations.

Exceptions to the agreement between modeled and observed HO_x occur at high solar zenith angles (SZA) (model underestimates by up to a factor of 5) and inside cirrus clouds (model overestimates by up to a factor of 2). In these 2 cases we propose a possible role of heterogeneous chemistry: (1) heterogeneous conversion of NO_2 to HONO in aerosols (γ_{NO2} = 10^{-3}) during the night followed by photolysis of HONO could explain the discrepancy at sunrise and, (2) heterogeneous loss of HO_2 on ice crystals (γ_{ice_HO2} = 0.025) could explain the discrepancy inside cirrus clouds. Uncertainties in the kinetics of HNO_4 production and loss are an alternative explanation for the observations at high SZA [*Brune et al.*, 1999; *Wennberg et al.*, 1999]. The model also underestimates the observed HO_x during daytime for high levels of NO_x (>200 pptv). Possible explanations include the presence of unmeasured HO_x precursors (such as higher aldehydes) due to recent convection, or an incomplete understanding of HO_x chemistry under high NO_x conditions [*Faloona et al.*, this issue].

We find that the primary sources of HO_x from $O(^1D)+H_2O$ and from acetone photolysis are of similar magnitude for the SONEX conditions. Photolysis of acetone dominated when water vapor fell below 100 ppmv. The relative importance of HO_x sources from convective injection of peroxides was found to be of smaller importance during SONEX compared to previous campaigns [*Jaeglé et al.*, 1997, 1998] because of the larger concentrations of H_2O. The sink of HO_y (= HO_x + 2
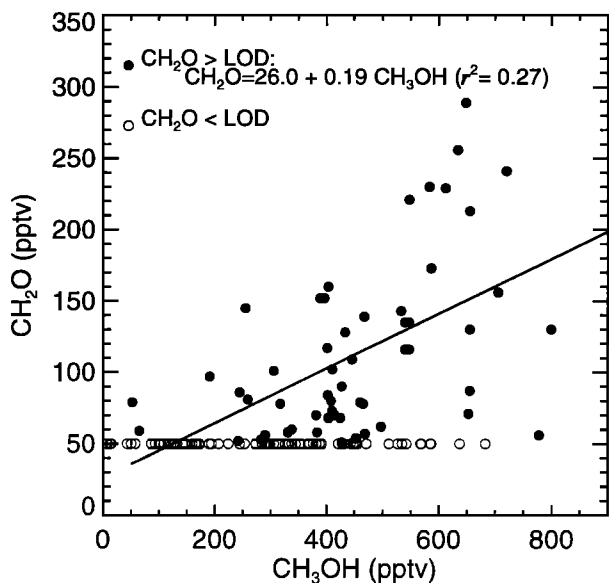
Figure 9. Correlation between observations of CH_2O and methanol, CH_3OH, at 8-12 km altitude. CH_2O observations below the LOD (<50 pptv) are shown by open circles, and observations above the LOD are shown by solid circles. A regression line is shown for observations above the LOD.

$H_2O_2 + 2$ $CH_3OOH + HNO_2 + HNO_4$) was dominated by $OH+HO_2$ for $NO_x<50$ pptv and by $OH+HNO_4$ for $NO_x>50$ pptv. Under most conditions in SONEX (median $NO_x \sim 90$ pptv), the reaction $OH+HNO_4$ was the principal sink of HO_x.

Heterogeneous conversion of HO_2 to H_2O_2 on aerosols (included in our standard model with $\gamma_{HO2} = 0.2$) is found to be of comparable magnitude to the gas-phase source of H_2O_2. With this source, production and loss of H_2O_2 are in rough balance. Observations of CH_3OOH are systematically underestimated by chemical steady state model calculations. Convective influence and uncertainty in the rate constant for the $HO_2+CH_3O_2$ reaction may both contribute to this discrepancy.

The majority of CH_2O observations at 8-12 km were below the 50 pptv limit of detection (LOD) of the instrument, consistent with model values which predict 30-60 pptv for the SONEX conditions. However, 45% of the CH_2O observations were above the LOD and occasionally very high (up to 350 pptv). The model does not capture these high concentrations nor their variability. High CH_2O in the observations is associated with high CH_3OH and with cirrus clouds, suggesting a possible source of CH_2O from heterogeneous conversion of CH_3OH on aerosols and ice crystals.

The set of measurements collected during SONEX demonstrates that current models can reproduce the fast photochemistry of HO_x radicals in the upper troposphere to within the uncertainty in the observations, and can also account for the observed variance in HO_2 concentrations. These results lend some confidence in our ability to assess the effects of aircraft NO_x emissions on ozone in that region of the atmosphere. Despite this overall good agreement, major uncertainties remain regarding (1) the sources of HO_x at sunrise and sunset, (2) heterogeneous HO_x chemistry in aerosols and cirrus clouds, (3) the sources of CH_2O and

CH_3OOH, (4) HO_x-NO_x chemistry for high NO_x conditions [*Faloona et al.*, this issue], and (5) HNO_4 reaction kinetics [*Brune et al.*, 1999].

References

Anderson, B.E., et al., An assessment of aircraft as a source of particles to the upper troposphere, *Geophys. Res. Lett.*, 26, 3069-3072, 1999.

Atkinson, R., et al., Evaluated kinetic and photochemical data for atmospheric chemistry - Supplement VI, *J. Phys. Chem. Ref. Data*, 26, 1329-1499, 1997.

Brune, W.H., et al., Airborne in situ OH and HO2 observations in the cloud-free troposphere and lower stratosphere during SUCCESS, *Geophys. Res. Lett.*, 25, 1701-1704, 1998.

Brune, W.H., et al., OH and HO2 chemistry in the north Atlantic free troposphere, *Geophys. Res. Lett.*, 26, 3077-3080, 1999.

Chatfield, R.B., and P.J. Crutzen, Sulfur dioxide in remote oceanic air: Cloud transport of reactive precursors, *J. Geophys. Res.*, 89, 7111-7132, 1984.

Clarke, A.D., Atmospheric nuclei in the remote free troposphere, *J. Atmos. Chem.*, 14, 479-488, 1992.

Cohan, D.S., M.G. Schultz, D.J. Jacob, B.G. Heikes, and D.R. Blake, Convective injection and photochemical decay of peroxides in the tropical upper troposphere: Methyl iodide as a tracer of marine convection, *J. Geophys. Res.*, 104, 5717-5724, 1999.

Cooper, P.L., and J.P.D. Abbatt, Heterogeneous interactions of OH and HO2 radicals with surfaces characteristics of atmospheric particulate matter, *J. Phys. Chem.*, 100, 2249-2254, 1996.

Crawford, J., et al., Assessment of upper tropospheric HO_x sources over the tropical Pacific based on NASA GTE/PEM data: Net effect on HO_x and other photochemical parameters, *J. Geophys. Res.*, 104, 16255-16273, 1999.

Cziczo, D.J., and J.P.D. Abbatt, Deliquescence, efflorescence, and supercooling of ammonium sulfate aerosols at low temperature: Implications for cirrus cloud formation and aerosol phase in the atmosphere, *J. Geophys. Res.*, 104, 13781-13790, 1999.

DeMore, W.B., et al., Chemical kinetics and photochemical data for use in stratospheric modeling, *JPL Publ.*, 97-4, 1997.

Dransfield, T.J., K.K. Perkins, N.M. Donahue, J.G. Anderson, M.M. Sprengnether, and K.L. Demerjian, Temperature and pressure dependent kinetics of the gas-phase reaction of the hydroxyl radical with nitrogen dioxide, *Geophys. Res. Lett.*, 26, 687-690, 1999.

Faloona, I., D. Tan, and W.H. Brune, In-situ observations of the influence of clouds on OH and HO2 concentrations throughout the troposphere, paper presented at Conference on the Atmospheric Effects of Aviation, Atmospheric Effects of Aviation Project, Virginia Beach, Va., 1998.

Faloona, I., et al., Observations of HO_x and its relationship with NO_x in the upper troposphere during SONEX, *J. Geophys. Res.*, this issue.

Folkins, I., P.O. Wennberg, T.F. Hanisco, J.G. Anderson, and R.J. Salawitch, OH and HO2 in two biomass burning plumes: Sources of HO_x and implications for ozone production, *Geophys. Res. Lett.*, 24, 3185-3188, 1997.

Fuelberg, H. E. et al., A meteorological overview of the SONEX period, *J. Geophys. Res.*, this issue.

Gerber, H., C.H. Twohy, B. Gandrud, A.J. Heymsfield, G.M. McFarquhar, P.J. DeMott, and D.C. Rogers, Measurements of wave-cloud microphysical properties with two new aircraft probes, *Geophys. Res. Lett.*, 25, 1117-1120, 1998.

Gierczak, T., J.B. Burkholder, S. Bauerle, and A.R. Ravishankara, Photochemistry of acetone under tropospheric conditions, *Chem. Phys.*, 231, 229-244, 1998.

Grant, W.B., et al., A case study of transport of tropical marine boundary layer and lower tropospheric air masses to the northern midlatitude upper troposphere, *J. Geophys. Res.*, this issue.

Gregory, G.L., C.H. Hudgins, and R.A. Edhal Jr., Laboratory evaluation of an airborne ozone instrument that compensates for altitude/sensitivity effects, *Environ. Sci. Technol.*, 17, 100-103, 1983.

Hagen, D.E., M.B. Trueblood, and P.D. Whitefield, A field sampling of jet exhaust aerosols, *Particle Sci. and Techn.*, *10*, 53-63, 1992.

Hanson, D.R., J.B. Burkholder, C.J. Howard, and A.R. Ravishankara, Measurement of OH and HO$_2$ radical uptake coefficients on water and sulfuric acid surfaces, *J. Phys. Chem.*, *96*, 4979-4985, 1992.

Heikes, B., et al., Ozone, hydroperoxides, oxides of nitrogen, and hydrocarbon budgets in the marine boundary layer over the South Atlantic, *J. Geophys. Res.*, *101*, 24,221-24,234, 1996.

Jacob, D.J., Heterogeneous chemistry and tropospheric ozone, *Atmos. Environ.*, in press, 1999.

Jacob, D.J., et al., The origin of ozone and NO$_x$ in the tropical troposphere: A photochemical analysis of aircraft observations over the South Atlantic Basin, *J. Geophys. Res.*, *101*, 24,235-24,250, 1996.

Jaeglé, L., et al., Observations of OH and HO$_2$ in the upper troposphere suggest a strong source from convective injection of peroxides, *Geophys. Res. Lett.*, *24*, 3181-3184, 1997.

Jaeglé, L., D.J. Jacob, W.H. Brune, D. Tan, I. Faloona, A.J. Weinheimer, B.A. Ridley, T.L. Campos, and G.W. Sachse, Sources of HO$_x$ and production of ozone in the upper troposphere over the United States, *Geophys. Res. Lett.*, *25*, 1705-1708, 1998.

Jaeglé, L., et al., Ozone production in the upper troposphere and the influence of aircraft during SONEX: Approach of NO$_x$-saturated conditions, *Geophys. Res. Lett.*, *26*, 3081-3084, 1999.

Jenkin, M.E., R.A. Cox, and D.J. Williams, Laboratory studies of the kinetics of formation of nitrous acid from the thermal reaction of nitrogen dioxide and water vapor, *Atmos. Environ.*, *22*, 487-498, 1988.

Kondo, Y., et al., Impact of aircraft emissions on NO$_x$ in the lowermost stratosphere at northern midlatitudes, *Geophys. Res. Lett.*, *26*, 3065-3068, 1999.

Lee, M., B.C. Noone, D. O'Sullivan, and B.G. Heikes, Method for the collection and HPLC analysis of hydrogen peroxide and C$_1$ and C$_2$ hydroperoxides in the atmosphere, *J. Atmos. Oceanic Technol.*, *12*, 1060-1070, 1995.

Levy, H., II, Photochemistry of the lower troposphere, *Planet. Space Sci.*, *20*, 919-935, 1972.

Logan, J.A., Trends in the vertical distribution of ozone: An analysis of ozonesonde data, *J. Geophys. Res.*, *99*, 25,553-25,585, 1994.

Logan, J.A., et al., Tropospheric chemistry: A global perspective, *J. Geophys. Res.*, *86*, 7210-7254, 1981.

Martin, S.T., Phase transformations for the ternary system (NH$_4$)$_2$SO$_4$-H$_2$SO$_4$-H$_2$O and the implications for cirrus cloud formation, *Geophys. Res. Lett.*, *25*, 1657-1660, 1998.

McKeen, S.A., T. Gierczak, J.B. Burkholder, P.O. Wennberg, T.F. Hanisco, E.R. Keim, R.-S. Gao, S.C. Liu, A.R. Ravishankara, and D.W. Fahey, The photochemistry of acetone in the upper troposphere: A source of odd-hydrogen radicals, *Geophys. Res. Lett.*, *24*, 3177-3180, 1997.

Müller, J.-F., and G. Brasseur, Sources of upper tropospheric HO$_x$: A three-dimensional study, *J. Geophys. Res.*, *104*, 1705-1715, 1999.

Parrish, D.D., M. Trainer, J.S. Holloway, J.E. Yee, G.L. Forbes, and J.L. Moody, Relationships between ozone and carbon monoxide at surface sites in the north Atlantic region, *J. Geophys. Res.*, *103*, 13,357-13,376, 1998.

Prather, M.J., and D.J. Jacob, A persistent imbalance in HO$_x$ and NO$_x$ photochemistry of the upper troposphere driven by deep tropical convection, *Geophys. Res. Lett.*, *24*, 3189-3192, 1997.

Pueschel, R.F., S. Verman, H. Rohatschek, N. Bojadieva, G.V. Ferry, D. Allen, and S.D. Howard, Vertical transport of anthropogenic soot aerosol into the middle atmosphere, *J. Geophys. Res.*, this issue.

Sachse, G.W., J.E. Collins, G.R. Hill, L.O. Wade, L.G. Burney, and J.A. Ritter, Airborne tunable diode laser sensor for high-precision concentration and flux measurements of carbon monoxide and methane, *Proc. SPIE Int. Soc. Opt. Eng.*, *1433*, 145-156, 1991.

Schultz, M., et al., On the origin of tropospheric ozone and NO$_x$ over the tropical South Pacific, *J. Geophys. Res.*, *104*, 5829-5843, 1999.

Shetter, R.E., and M. Müller, Photolysis frequency measurements using actinic flux spectroradiometry during the PEM-Tropics mission: Instrumentation description and some results, *J. Geophys. Res.*, *104*, 5647-5661, 1999.

Simpson, I.J., et al., Nonmethane hydrocarbon measurements in the north Atlantic flight corridor during SONEX, *J. Geophys. Res.*, this issue.

Singh, H.B., A.M. Thompson, and H. Schlager, SONEX airborne mission and coordinated POLINAT 2 activity: Overview and accomplishments, *Geophys. Res. Lett.*, *26*, 3053-3056, 1999.

Singh, H.B., et al., High concentrations and photochemical fate of oxygenated hydrocarbons in the global troposphere, *Nature*, *378*, 50-54, 1995.

Singh, H.B., et al., Distribution and fate of selected oxygenated organic species in the troposphere and lower stratosphere over the Atlantic, *J. Geophys. Res.*, this issue.

Stevens, P.S., J.H. Mather, and W.H. Brune, Measurement of tropospheric OH and HO$_2$ by laser-induced fluorescence at low-pressure, *J. Geophys. Res.*, *99*, 3543-3557, 1994.

Talbot, R.W., J.E. Dibb, E.M. Scheuer, D.R. Blake, N.J. Blake, G.L. Gregory, G.W. Sachse, J.D. Bradshaw, S.T. Sandholm, and H.B. Singh, Influence of biomass combustion emissions on the distribution of acidic trace gases over the southern Pacific basin during austral springtime, *J. Geophys. Res.*, *104*, 5623-5634, 1999.

Talbot, R.W., et al., Reactive nitrogen budget during the NASA SONEX mission, *Geophys. Res. Lett.*, *26*, 3057-3060, 1999.

Talukdar, R.K., C.A. Longfellow, M.K. Gilles, and A.R. Ravishankara, Quantum yields of O(^{1}D) in the photolysis of ozone between 289 and 329 nm as a function of temperature, *Geophys. Res. Lett.*, *25*, 143-146, 1998.

Thompson, A.M., L.C. Sparling, Y. Kondo, B.E. Anderson, G.L. Gregory, and G.W. Sachse, Perspectives on NO, NO$_y$ and fine aerosol sources and variability during SONEX, *Geophys. Res. Lett.*, *26*, 3073-3076, 1999.

Vay, S.A., B.E. Anderson, G.W. Sachse, J.E. Collins, J.R. Podolske, C.H. Twohy, B. Gandrud, K.R. Chan, S.L. Baughcum, and H.A. Wallio, DC-8-based observations of aircraft CO, CH$_4$, N$_2$O, and H$_2$O(g) emission indices during SUCCESS, *Geophys. Res. Lett.*, *25*, 1717-1720, 1998.

Wennberg, P.O., et al., Hydrogen radicals, nitrogen radicals and the production of ozone in the middle and upper troposphere, *Science*, *279*, 49-53, 1998.

Wennberg, P.O., et al., Twilight observations suggest unknown sources of HO$_x$, *Geophys. Res. Lett.*, *26*, 1373-1376, 1999.

B. Anderson, G. L. Gregory, and G. W. Sachse, NASA Langley Research Center, Hampton, VA 23681.

D. R. Blake, Department of Chemistry, University of California, Irvine, CA 92717.

W. B. Brune, I. Faloona, D. Tan, Department of Meteorology, Pennsylvania State University, University Park, PA 16802.

G. Ferry, R. Pueschel, and H. B. Singh, NASA Ames Research Center, Moffett Field, CA 94035.

B. G. Heikes, Graduate School of Oceanography, University of Rhode Island, Narragansett, RI 02882.

D. J. Jacob and L. Jaeglé (corresponding author), Division of Engineering and Applied Sciences and Department of Earth and Planetary Sciences, Harvard University, 29 Oxford Street, Pierce Hall, Cambridge, MA 02138. (e-mail: lyj@io.harvard.edu)

Y. Kondo, Solar Terrestrial Environment Laboratory, Nagoya University, Nagoya, Japan.

R. E. Shetter, National Center for Atmospheric Research, Boulder, CO 80303.